

Comparison Between Ambient Vibrations H/V Obtained from the Diffuse Field and Distributed Surface Sources Models



A. García-Jerez

IAGPDS, Universidad de Granada, Spain

F. Luzón

Departamento de Física Aplicada, Universidad de Almería, Spain

D. Albarello & E. Lunedei

Dipartimento di Scienze della Terra, Università degli Studi di Siena, Italy

M. A. Santoyo

Universidad Complutense de Madrid, Spain

L. Margerin

Observatoire Midi-Pyrénées, France

F. J. Sánchez-Sesma

Instituto de Ingeniería, UNAM, Mexico

SUMMARY:

Two methods for forward computation of H/V spectral ratio of ambient vibrations based on different hypotheses are compared in this work. The first one rests on the Diffuse Field Approach (DFA), assuming that the relative power of each wave type is prescribed by the energy equipartition principle; under this hypothesis, the proportionality between the Fourier-transformed autocorrelation (power spectrum), at any point of the medium, and the imaginary part of the Green's function, when source location corresponds to the receiver location, holds. The second method assumes that the ambient vibration wavefield is generated by Distributed Surface point-like aleatory independent Sources (DSS hypothesis), which effects propagates to the receiver without significant scattering, apart from the one due to the layering. These models have been numerically compared for a set of simple structures. An algorithm for calculation of DFA spectral ratios based on a classical contour integration in the complex radial-wavenumber plane is also outlined.

Keywords: Ambient vibration prospecting, H/V spectral ratio, Numerical simulations

1. INTRODUCTION

The H/V spectral ratio (Nakamura, 1989) is a widely used technique of seismic exploration which can be employed as a tool for quick detection and evaluation of site effects in terms of *SH*-resonance frequency as well as for constraining the elastic properties of the shallow geological structure (usually under the assumption of horizontally layered medium). Nevertheless, some controversial aspects about the exact physical interpretation of the outcome of this technique (H/V curve) remain. Most of them are related with the nature of the ambient vibration wavefield and its sources. These differences in the forward modelling of H/V ratio might have consequences in the results of ground model inversions, which should be thoroughly studied.

In this work, we compare two possible interpretations of H/V ratios with solid theoretical foundations. The hereafter called DSS hypothesis assumes that the wavefield is generated by a set of Distributed Surface point-like aleatory independent Sources, which effects propagate to the receiver without significant scattering, apart from the waveguide effects of layering (Lunedei & Albarello, 2010). On the other hand, Nakamura's ratios can be evaluated by considering the Diffuse Field Approach (DFA), which assumes that the relative power of each type of wave is prescribed by the energy equipartition principle. Under this hypothesis, the proportionality between the Fourier-transformed autocorrelation

(power spectrum), at any point of the medium, and the imaginary part of the Green's function, when source location corresponds to the one of the receiver, holds (Sánchez-Sesma *et al.*, 2011a). The assumption of a major role of multiple scattering is behind this formulation. A suitable method for calculation of DFA spectral ratios based on a classical contour integration in the complex radial-wavenumber plane is also presented. The imaginary part of the Green's function at source is synthesized as a sum of residue contributions (surface waves) and branch-line integrations (body waves) over a bounded interval only (from $k = 0$ up to the wavenumber of S-waves in the halfspace).

2. THE H/V SPECTRAL RATIO AS DESCRIBED BY DFA

If a 3D diffuse, equipartitioned, harmonic displacement vector field $u_i(\mathbf{x}, \omega)$ is established within an elastic medium, the average cross-correlations of motions at points \mathbf{x}_A and \mathbf{x}_B can be written (*e. g.* Perton *et al.*, 2009) as:

$$\langle u_i(\mathbf{x}_A, \omega) u_j^*(\mathbf{x}_B, \omega) \rangle = -2\pi E_S k_S^{-3} \text{Im}[G_{ij}(\mathbf{x}_A; \mathbf{x}_B; \omega)] \quad (2.1)$$

where the $G_{ij}(\mathbf{x}_A, \mathbf{x}_B, \omega)$ is the Green's function, ω the circular frequency, $k_S = \omega/V_S$ the shear wave number, V_S the shear wave propagation velocity, E_S the average energy density of shear waves, which is a measure of the strength of the diffuse illumination. Eqn. 2.1 is the analytical consequence of a correlation-type elastic representation theorem and has been verified in canonical examples of a full space (Sánchez-Sesma & Campillo, 2006) and for elastic inclusions (Sánchez-Sesma *et al.*, 2006, 2008).

The energy density at point \mathbf{x}_A along the direction m can be obtained if we rewrite Eqn. 2.1 assuming $\mathbf{x}_A = \mathbf{x}_B$:

$$P_m(\mathbf{x}_A, \omega) \equiv \langle u_m(\mathbf{x}_A, \omega) u_m^*(\mathbf{x}_A, \omega) \rangle = -2\pi E_S k_S^{-3} \text{Im}[G_{mm}(\mathbf{x}_A; \mathbf{x}_A; \omega)], \text{ no sum.} \quad (2.2)$$

Thus, the total energy density at a point, $\sum_m P_m$, is proportional to the imaginary part of the trace of the Green's tensor for coincident receiver and source. The imaginary part of, say, G_{11} represents the power injected by the unit harmonic load in direction 1. This quantity "detects" energies that are both radiated and coming back to the source and may be used for imaging. Finally, we can thus write the H/V ratio as:

$$[H/V](\omega) \equiv \sqrt{\frac{P_1 + P_2}{P_3}} = \sqrt{\frac{2\text{Im}[G_{11}(\mathbf{x}; \mathbf{x}; \omega)]}{\text{Im}[G_{33}(\mathbf{x}; \mathbf{x}; \omega)]}}, \quad (2.3)$$

where P_1 , P_2 and P_3 are the directional energy densities for the horizontal (P_1 and P_2) and the vertical (P_3) degrees of freedom. The last step includes an assumption of a pure 1D configuration (horizontal layering), where horizontal directions are indistinguishable (*i. e.*, $P_1 = P_2$). Eqn. 2.3 links average measurements expressed on the left side with an intrinsic property of the medium on the right, and naturally allows for the inversion of H/V ratio accounting for the contributions of Rayleigh, Love and body waves.

2.1. Surface Wave Contribution

Several studies have shown that surface waves represent the dominant contribution to the wavefield at large enough frequencies. In that case, we can rewrite the Green's Functions in terms of their well-known modal characteristics. After taking the zero-distance limit of the Harkrider's (1964) expressions for a horizontally layered medium, the surface-wave version of Eqn. 2.2 can be expressed

as:

$$P_1 = P_2 \propto -\text{Im}[G_{11}(\mathbf{x}; \mathbf{x}; \omega)] \rightarrow \frac{1}{4} \sum_m \{A_{Rm} \chi_m^2 + A_{Lm}\}, \quad (2.4)$$

$$P_3 \propto -\text{Im}[G_{33}(\mathbf{x}; \mathbf{x}; \omega)] \rightarrow \frac{1}{2} \sum_m A_{Rm}, \quad (2.5)$$

where A_{Rm} and A_{Lm} represent the medium response of Rayleigh and Love waves for the m -th mode (Harkrider, 1964) and χ_m the corresponding Rayleigh wave ellipticity (as a real quantity).

3. THE H/V SPECTRAL RATIO AS DESCRIBED BY DSS

In this approach it is accepted that ambient vibrations are generated by a continuum of surface loads distributed on the Earth free surface. The ground motion they produce propagates to the receiver without significant scattering, except for the one due to the stratigraphical interfaces (impedance contrasts). This model was formulated under the assumption of weakly dissipative medium, for both the full ambient vibration wavefield (Lunedei & Albarello, 2010) and for the surface-wave component only (Lunedei & Albarello, 2009). Adapting their expressions to the usual Green's function nomenclature in Cartesian coordinates, we find:

$$P_1(\omega) + P_2(\omega) = \pi\sigma^2 \int_{x_{\min}}^{\infty} \left[(\sigma_1^2 + \sigma_2^2) \left(|G_{11}(0; x_1, 0; \omega)|^2 + |G_{22}(0; x_1, 0; \omega)|^2 \right) + 2\sigma_3^2 |G_{13}(0; x_1, 0; \omega)|^2 \right] x_1 dx_1, \quad (3.1)$$

$$P_3(\omega) = \pi\sigma^2 \int_{x_{\min}}^{\infty} \left[(\sigma_1^2 + \sigma_2^2) |G_{31}(0; x_1, 0; \omega)|^2 + 2\sigma_3^2 |G_{33}(0; x_1, 0; \omega)|^2 \right] x_1 dx_1, \quad (3.2)$$

where σ^2 stands for the total surface variance density of random sources and σ_j^2 for j -component relative surface variance density as defined by Lunedei & Albarello (2010). The separate expressions of $P_1(\omega)$ and $P_2(\omega)$ in the case of anisotropic illumination ($\sigma_1 \neq \sigma_2$) have been also determined in the quoted paper. Formulae in Eqn. 3.1-2, which have been derived under a rigorous statistical framework, generalize the Field & Jacob (1993) expressions, enabling different weights of Green's functions. A source-free circular area with radius $x_{\min} > 0$ surrounding the receiver can be eventually considered in this calculation (this area is absent when $x_{\min} = 0$). Finally, the spectral ratio is calculated as:

$$[H/V](\omega) \equiv \sqrt{\frac{P_1(\omega) + P_2(\omega)}{P_3(\omega)}}. \quad (3.3)$$

3.1. Surface Wave Contribution

In the case of predominance of surface waves, expressions in Eqns. 3.1-2 assume a simpler form. Compact formulae were first given by Arai & Tokimatsu (2004) for an elastic stratified medium, under some additional simplifying hypotheses (asymptotic long-distance forms of the Green functions, suitable free-of-sources areas, incoherent summation of modal contributions):

$$P_1(\omega) + P_2(\omega) = \frac{\kappa}{2} \sigma^2 \sum_{m \in \text{RAYLEIGH}} \left[2\sigma_3^2 + \chi_m^2 (\sigma_1^2 + \sigma_2^2) \right] \left(\frac{A_{Rm}}{k_{Rm}} \right)^2 \chi_m^2 +$$

$$+ \frac{\kappa}{2} \sigma^2 \sum_{m \in \text{LOVE}} (\sigma_1^2 + \sigma_2^2) \left(\frac{A_{Lm}}{k_{Lm}} \right)^2, \quad (3.4)$$

$$P_3(\omega) = \frac{\kappa}{2} \sigma^2 \sum_{m \in \text{RAYLEIGH}} \left[2\sigma_3^2 + \chi_m^2 (\sigma_1^2 + \sigma_2^2) \right] \left(\frac{A_{Rm}}{k_{Rm}} \right)^2, \quad (3.5)$$

where κ is a frequency independent damping parameter, representative of the scattering effect. Under the same simplifying hypotheses, Lunedei & Albarello (2009) proposed a different implementation, which includes the effects of material damping (viscosity):

$$P_1(\omega) + P_2(\omega) = \frac{\sigma^2}{4} \sum_{m \in \text{RAYLEIGH}} \left[2\sigma_3^2 + \chi_m^2 (\sigma_1^2 + \sigma_2^2) \right] \chi_m^2 \frac{(A_{Rm})^2}{k_{Rm} \alpha_{Rm}} \exp(-2\alpha_{Rm} x_{\min}) + \frac{\sigma^2}{4} \sum_{m \in \text{LOVE}} \frac{(A_{Lm})^2}{k_{Lm} \alpha_{Lm}} \exp(-2\alpha_{Lm} x_{\min}), \quad (3.6)$$

$$P_3(\omega) = \frac{\sigma^2}{4} \sum_{m \in \text{RAYLEIGH}} \left[2\sigma_3^2 + \chi_m^2 (\sigma_1^2 + \sigma_2^2) \right] \frac{(A_{Rm})^2}{k_{Rm} \alpha_{Rm}} \exp(-2\alpha_{Rm} x_{\min}), \quad (3.7)$$

where α_{Lm} and α_{Rm} are the attenuation factors for the m -th Love and Rayleigh mode respectively, which depend on the viscous properties of the medium (*i.e.*, P- and S-wave damping factors or corresponding quality factors). These formulae explicitly depend on the source-free area radius $x_{\min} \geq 0$, which can be set as a constant value, as well as a frequency dependent function.

4. SYNTHETIC TESTS

In order to study the differences and similarities of these two methods in practice, a set of synthetic tests has been performed using the stratigraphic models listed in Table 4.1. Models M1* (purely elastic) were used by Tuan *et al.* (2011) in their studies on the Rayleigh waves ellipticity. Stratigraphic model M2 has been taken from Albarello & Lunedei (2011), as well as the M2* model family, which elements are generated from M2 varying either the Poisson's ratio of the upper layer or the S-wave velocity of the intermediate one. All these models basically consist of a layer overlying a half-space, although models M2* include a thick buffer layer (the intermediate one), which prevents from sharply unrealistic truncation of surface-wave higher modes in the range of frequency of interest (0.5-20 Hz). Finally, model M3, taken from Sánchez-Sesma *et al.* (2011b), has the particularity of presenting two significant impedance contrasts.

Table 4.1. Models used in the numerical experiments

M1*					
$4h/V_{S1}$ (s)	V_S / V_{S2}	ν	ρ/ρ_2	Q_P	Q_S
1	0.05-0.50	0.00-0.45	0.7391	∞	∞
∞	1	0.3449	1	∞	∞
M2					
h (m)	V_S (m/s)	ν	ρ (g/cm ³)	Q_P	Q_S
25	200	0.333	1.9	500	500
5000	1000	0.333	2.5	500	500
∞	2000	0.257	2.5	500	500
M2*					
h (m)	V_S (m/s)	ν	ρ (g/cm ³)	Q_P	Q_S
25	200	0.01-0.49	1.9	500	500
5000	228-1520	0.333	2.5	500	500
∞	2000	0.257	2.5	500	500

M3						
h (m)	V_S (m/s)	V_P (m/s)	ρ/ρ_4	Q_P	Q_S	
5	30	500	1	500	500	
25	100	500	1	500	500	
50	150	500	1	500	500	
∞	500	1500	1	500	500	

4.1. DFA Main Peak Characteristics for a Layer over Halfspace

A set of 100 H/V calculations have been carried out for the simple models in the set M1*. In order to study the main peak shape, which can be potentially affected by body wave contributions, full wavefield simulation was used. Results confirm a good match between the peak frequency and the fundamental resonance of vertically incident S-waves (f_{0SH}). Some deviations (of up to about 12% towards lower frequencies) have been found for models with low velocity contrasts (~ 2 in V_S) and low Poisson's ratio in the layer (upper left corner in Fig. 1a). Nevertheless, we find that the amplitude of the H/V ratio is not predictive of the SH transfer function amplitude (Fig 1b) and their ratio strongly depends both on the impedance contrast and the Poisson's ratio. It should be noted that the compared amplitudes correspond to slightly different frequencies.

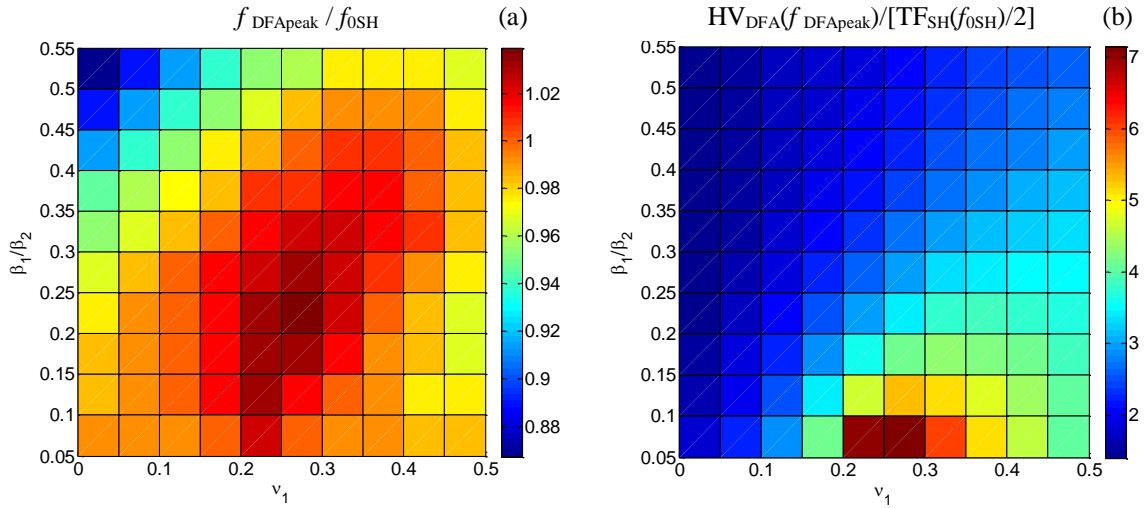


Figure 1. Main peak characteristics for the M1* set of models using full-wavefield DFA simulations: (a) peak frequency to f_{0SH} ratio; (b) peak amplitude ratios between DFA simulations and the vertical S-wave semi-transfer function.

4.2. Overall H/V Shapes for a Layer over Halfspace Using Surface Waves

The differences between these two approaches emerge in a more explicit form if their versions for surface waves are compared (Eqn. 2.4-5 vs. 3.4-5 and 3.6-7). Formulae have a similar structure, but the contributions of each seismic phase and mode to the total power differ. In fact, it depends on $A_{\bullet m}$

in the DFA formulation and on $\left(\frac{A_{\bullet m}}{k_{\bullet m}}\right)^2$ or $\frac{(A_{\bullet m})^2}{k_{\bullet m} \alpha_{\bullet m}} \exp(-2\alpha_{\bullet m} x_{\min})$ in the DSS one, where “ \bullet ” indicates

either Love (L) or Rayleigh (R) phases. Square operator in the last model is a consequence of the power computation, which is proportional to the ground motion square; in the DFA model, the correct physical dimension is insured by the energy factor that multiplies the imaginary part of the Green's function in Eqn. 2.2. So, while in the DSS the energy repartition among contributing waves depends on the relative energies (expressed by square amplitude) of the waves received from the surface source distribution, in the DFA this repartition it is established by the Green's function for coincident source and receiver. This is a very important physical difference between our two approaches. The common inverse wavenumber $1/k_{\bullet m}$ in the DSS formulae represents an effect of the long-range wave

propagation from the generic source to the receiver, while the other $1/k_{\bullet m}$ factor or the correspondent $1/\alpha_{\bullet m}$ is due to integration on the horizontal distance to compute the total source distribution effect. Both these elements are obviously absent in the DFA method.

It can be shown that in both the considered models, the H/V ratio restricted to surface-waves tends to the ellipticity of (non-dispersive) Rayleigh waves over a halfspace and depend on the characteristics of the deeper medium (say χ_{HS}) as $f \rightarrow 0$. This fact is due to the faster drop of the fundamental Love mode medium response A_{LO} in comparison with A_{RO} (specifically, $A_{LO} = O(k_{LO}^2)$ as $k_{LO} \rightarrow 0$ while $A_{RO} = O(k_{RO})$ as $k_{RO} \rightarrow 0$) together with the limits $\chi_0(f) \rightarrow \chi_{HS}$ and $k_{RO}/k_{LO} \rightarrow V_{SN}/V_{RN}$ as $f \rightarrow 0$ ($V_{SN} = S$ -wave velocity in the halfspace, $V_{RN} =$ Rayleigh-wave velocity for the halfspace).

The effects of different way of considering the modal contributions in the surface wave version of DFA and DSS (Eqn. 3.4-5) calculations have been investigated for models in M1*: Fig. 2 compares 25 synthetic H/V ratios calculated with both methods. For DSS calculations, the relative surface variance densities along the three Cartesian components were chosen to fulfil $\sigma_1^2 = \sigma_2^2 = \sigma_3^2/2$. Even though the overall shapes are very similar and peak frequencies match well, some differences are still revealed in this figure. The $[H/V]_{DSS}$ curves often show sharper peaks and troughs at frequencies higher than the fundamental S -wave resonance (*i.e.*, associated with higher modes) in comparison with their $[H/V]_{DFA}$ counterparts.

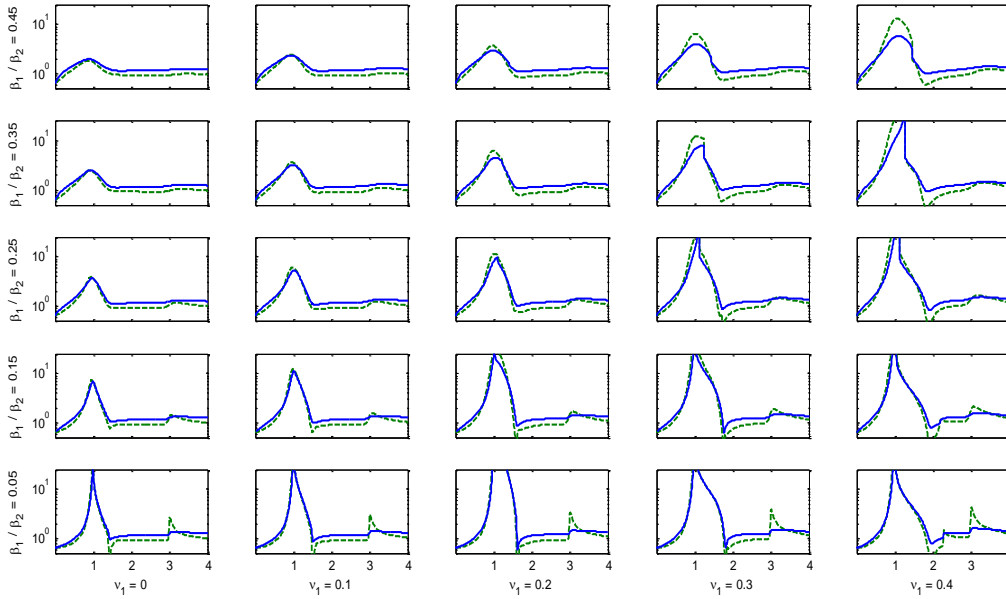


Figure 2. Solid blue line: $[H/V]_{DFA}$ vs. (f/f_{0SH}) using surface waves for some models in M1*. Dashed green line: respective $[H/V]_{DSS}$ vs. (f/f_{0SH}) curves following Arai & Tokimatsu (2004).

4.3. Surface-Wave and Body-Wave Contributions

Albarello & Lunedei (2011) have performed a detailed analysis of the influence of body and surface waves in the DSS frame for the model M2, which presents a single significant impedance contrast. They find significant contributions of body waves for frequencies around and below the S -wave resonance frequency f_{0SH} (2 Hz in this case), whereas surface waves clearly dominate for frequencies larger than the P -wave one f_{0P} (4 Hz in this case). This fact reflects on the deviation between blue (full wavefield, FW) and green (surface waves, SW) curves in Fig. 3a around the peak frequency. When a circular source-free area with a radius of 10 m exists (Fig. 3b), the FW produces an H/V peak equal to the one of the SW, probably as a consequence of the more efficient propagation of these last at long distances (see, *e.g.*, Tamura, 1996). The elastic DFA results show no difference between FW and SW H/V curve, which peak amplitude is less than the DSS one.

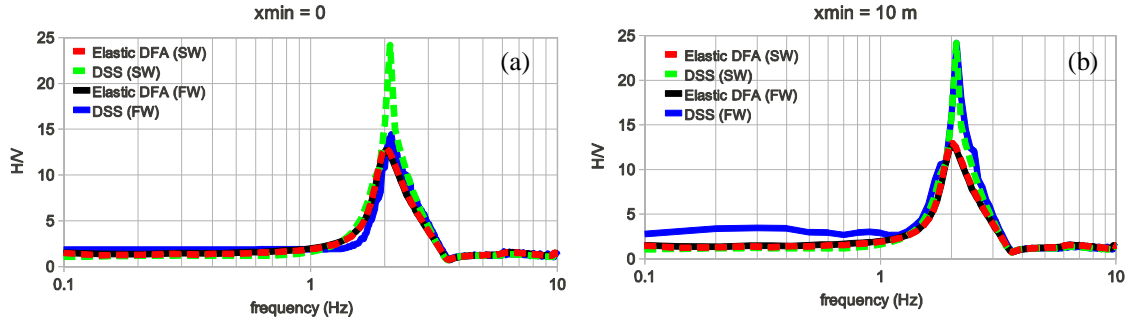


Figure 3. H/V ratios for structure M2 obtained by the DSS for full wavefield (blue) and the surface-wave component (green), as well as by the DFA for full wavefield (black) and the surface-wave component (red). (a) No source-free area is considered. (b) A source-free area with radius $x_{\min}=10$ m is set in the DSS method.

A parametric study of this stratigraphy is performed by considering the model family M2*, which full-wavefield results are shown in Fig. 4.

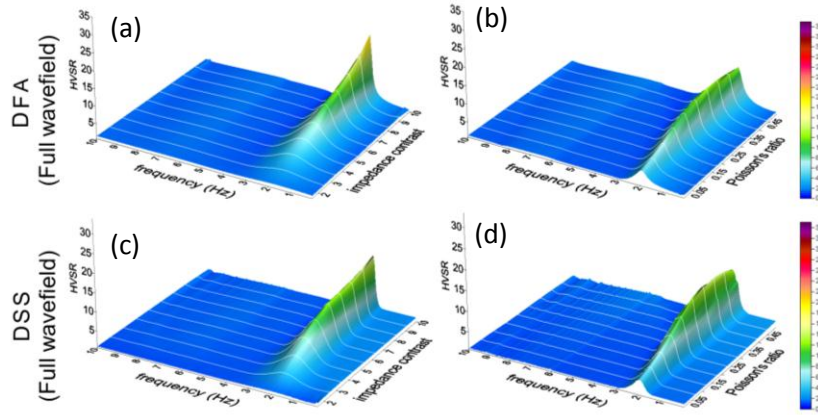


Figure 4. Panels (a) and (b): full-wavefield DFA spectral ratios for models in set M2*. Panels (c) and (d): respective counterparts obtained by using the DSS, with $x_{\min}=0$.

4.4. Differences between DFA and DSS in a More Complex Stratigraphic Model

By using model M3, which presents two important impedance contrasts at 5 and 80 m and a minor one at 30 m depth, we point out that, contrary to the single-layer case, remarkable differences in H/V shape deduced from DFA and DSS can occur for more complicated subsoil structures. Rough calculations from the S -wave travel-time lead to expected resonance frequencies of 1.5 and 0.33 Hz respectively for the principal contrasts and 0.6 for the secondary one. Two peaks appear in the elastic DFA computation near to 0.4 and 1.5 Hz (that can be associated with the two subsoil principal interfaces), for both the FW (black line in Fig. 5) and the SW cases (red line in Fig. 5). The DSS response is more complex. When no source-free area exists, the DSS-FW H/V (blue line in Fig. 5a) only shows the peak correspondent to the shallowest impedance contrast, while the other is retrieved by the DSS-SW counterpart (green line in Fig. 5a). Nevertheless, the main peak is recovered in the DSS-FW H/V curve if close sources are removed from the calculations, as Fig. 5b (blue line) shows for $x_{\min} = 5$ m, and moreover the overall shapes of the DFA-FW and DSS-FW curves approximately match. These results suggest that DFA and DSS might lead to closer results whenever a suitable source-free area is used in the DSS-FW computations, letting surface waves play a predominant role. The SW results seem very similar in any cases.

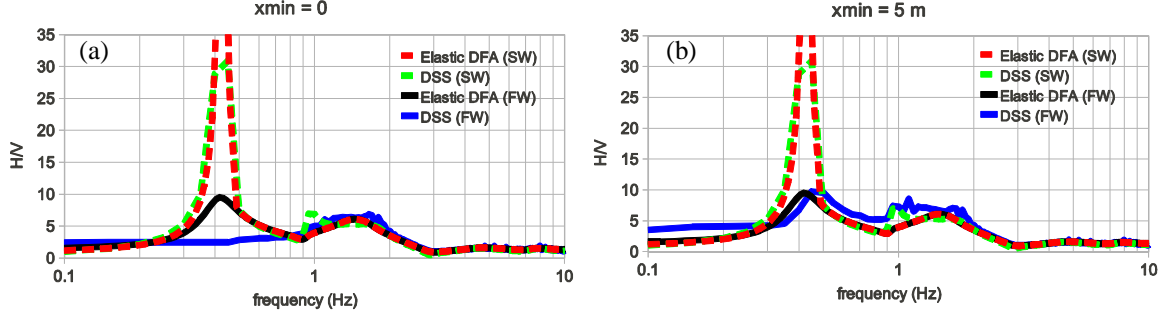


Figure 5. H/V ratios from DFA and DSS methods for model M3 (with $\sigma_1 = \sigma_2 = \sigma_3$): (a) surface loads are allowed on the whole ground surface; (b) near sources are removed from around the virtual station up to 5 m.

5. EFFICIENT CALCULATION OF H/V RATIOS UNDER THE DFA

A direct scheme for calculation of H/V ratios under the DFA has been proposed by Sánchez-Sesma *et al.* (2011a). Nevertheless, a more efficient one which takes advantage of complex wavenumber integrals can be performed as shown in this section. We may start rewriting the DFA equations in terms of the Green function in cylindrical coordinates:

$$[H/V](\omega) = \sqrt{2 \operatorname{Im}[q_0(r=0, \theta=0)] / \operatorname{Im}[w_0(r=0)]}, \quad (5.1)$$

with

$$\operatorname{Im}[w_0(r=0)] = \lim_{r \rightarrow 0} \operatorname{Im} \left[\frac{i}{2\pi} \int_0^{+\infty} f_{PSV}^V(k) J_0(kr) dk \right], \quad (5.2)$$

$$\operatorname{Im}[q_0(r=0, \theta=0)] = \lim_{r \rightarrow 0} \operatorname{Im} \left[\underbrace{\frac{i}{2\pi} \int_0^{+\infty} f_{SH}(k) \frac{J_1(kr)}{kr} dk}_{q_0^{SH}} + \frac{i}{4\pi} \int_0^{+\infty} f_{PSV}^H(k) [J_0(kr) - J_2(kr)] dk \right], \quad (5.3)$$

where $w_0(r)$ is the Fourier-transformed vertical displacement at horizontal distance r due to a delta-type vertical point load at the origin, while q_0 is the radial displacement at (r, θ) caused by a horizontal load in direction $\theta = 0$. Both source and receiver are located on the ground surface. The expressions of the functions $f_{PSV}^V(k)$, $f_{PSV}^H(k)$ and $f_{SH}(k)$ in terms of the quantities $G, H, J_L, K, L, M, N, R, S$ (defined, *e. g.* in Harkrider, 1964) are:

$$f_{PSV}^V(k) = -\frac{[GN - LH]}{[NK - LM]}, \quad f_{PSV}^H(k) = \frac{[RM - SK]}{[NK - LM]}, \quad f_{SH}(k) = \frac{(J_L)_{12} - (J_L)_{22}}{(J_L)_{21} - (J_L)_{11}}. \quad (5.4)$$

Using that these are odd functions of k , the integrals can be extended to the whole real axis replacing $J_n(kr)$ with $H_n^{(1)}(kr)/2$ and subsequently interpreted in the complex- k plane taking advantage of the integration contour shown in Fig. 6 (*e.g.* Tamura, 1996). The integrands present simple poles on the real axis as well as branch-cut discontinuities in the interval $[-\omega/V_{SN}, +\omega/V_{SN}]$ and along the whole imaginary axis due to the dependence on the square roots $v_{\omega N} = \sqrt{k^2 - (\omega/V_{PN})^2}$ and $v_{\beta N} = \sqrt{k^2 - (\omega/V_{SN})^2}$. The criteria used in this section for definition of Fourier transform and signs of $v_{\alpha j}$ and $v_{\beta j}$ in Eqs. 5.2-3 are same as in Aki and Richards (2002). In this manner, the original integrals are evaluated from the sum of residues (corresponding to Rayleigh and Love waves) and the branch-cut integrals in $[0, \omega/V_{SN}]$ and $[0, +i\infty)$ (corresponding to body waves).

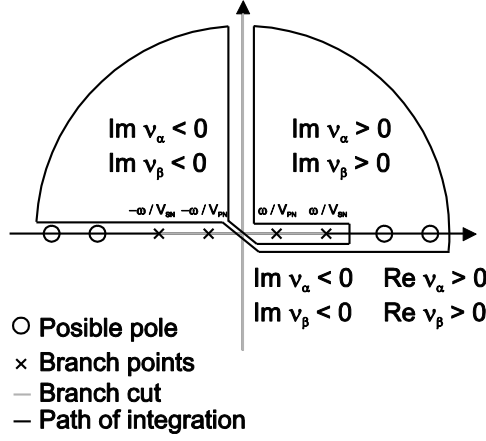


Figure 6. Contour used for complex-plane integration.

Nevertheless, due to the conjugation of $f_{PSV}^V(k)$, $f_{PSV}^H(k)$ and $f_{SH}(k)$ between both sides of the imaginary axis, integration in the latter interval will contribute to the real part of the Green's function only. Thus, and after taking the limit $r \rightarrow 0$, we finally obtain:

$$\text{Im}[w_0(r=0)] = -\frac{1}{2} \sum_{m \in \text{RAYLEIGH}} \text{Im}[\text{Resid}\{f_{PSV}^V(k)\}_{k=k_m}] + \frac{1}{2\pi} \int_0^{\omega/V_{SN}} \text{Re}[f_{PSV}^V(k)]_{4^{\text{th}}_{qu}} dk, \quad (5.5)$$

$$\text{Im}[q_0^{PSV}(r=0, \theta=0)] = -\frac{1}{4} \sum_{m \in \text{RAYLEIGH}} \text{Im}[\text{Resid}\{f_{PSV}^H(k)\}_{k=k_m}] + \frac{1}{4\pi} \int_0^{\omega/V_{SN}} \text{Re}[f_{PSV}^H(k)]_{4^{\text{th}}_{qu}} dk, \quad (5.6)$$

$$\text{Im}[q_0^{SH}(r=0, \theta=0)] = -\frac{1}{4} \sum_{m \in \text{LOVE}} \text{Im}[\text{Resid}\{f_{SH}(k)\}_{k=k_m}] + \frac{1}{4\pi} \int_0^{\omega/V_{SN}} \text{Re}[f_{SH}(k)]_{4^{\text{th}}_{qu}} dk. \quad (5.7)$$

The surface-wave part of these expressions matches Eqns. 2.4-5, once the definitions of medium responses and ellipticity are inserted. Note that the constraint of numerical integration to the range $[0, \omega/V_{SN}]$ and the separate calculation of surface and body waves represent the major improvements reached with this analysis. The precautions concerning possible poles at $k=0$ (see Wang & Herrmann, 1980) can be ignored in the limit $r \rightarrow 0$.

6. CONCLUSIONS

The results obtained indicate that both the DSS and the DFA provide reasonable full-wavefield and surface-wave synthetics for H/V spectral ratios. These curves present overall patterns in some extent similar, but not identical.

In spite of the rather different underlying hypotheses, DFA and DSS lead to similar H/V curves for models with a dominant impedance contrast (M1*, M2*). Relative H/V main peaks match the first SH resonance frequency (f_{0SH}) in a very good way. Nevertheless peak amplitudes may differ and show non-trivial dependence on the impedance contrast and the Poisson's ratio. Results relative to DSS also depend on the source distribution around the receiver. For both models, surface waves represent the dominant contribution at high enough frequencies, whereas body waves play an important role around and below f_{0SH} . The experiments performed for a stratigraphy with two important and a weak impedance contrasts show some variability in the overall shape of the H/V curve in the full-wavefield DSS when sources are present or absent near the receiver. DFA and DSS should lead to closer results whenever near sources were eliminated from the DSS computation and surface waves were playing the major role. This seems to suggest that, although physical bases are different, surface-wave behaviour described by DFA and DSS is very similar. In any case, the differences in the overall H/V

curve features make clear that the relationships between DFA and DSS still require further scrutiny. Finally, explicit expressions (using Harkrider's notation) for the surface-wavefield components of the DFA spectral densities have been provided and an efficient way for full-wavefield computing of DFA HV has been sketched.

ACKNOWLEDGEMENTS

This research was partially supported by the Spanish Comisión Interministerial de Ciencia y Tecnología project CGL2010-16250, by the European Union with Fondo Europeo de Desarrollo Regional, and by DGAP-UNAM, Mexico, under projects IN121709 and IN104712. The work done by A. G. J. was under contract Juan de la Cierva at University of Granada.

REFERENCES

- Aki, K. and Richards, P.G. (2002). *Quantitative Seismology*, Second Edition, University Science Books, Sausalito, CA.
- Albarelo, D. and Lunedei, E. (2011). Structure of an ambient vibration wavefield in the frequency range of engineering interest ([0.5, 20] Hz): insights from numerical modelling. *Near Surface Geophysics* **9**, doi:10.3997/1873-0604.2011017.
- Arai, H. and Tokimatsu, K. (2004). S-wave velocity profiling by inversion of microtremor H/V spectrum. *Bull. Seismol. Soc. Am.* **94**, 53-63.
- Field, E. and Jacob, K. (1993). The theoretical response of sedimentary layers to ambient noise. *Geophys. Res. Lett.* **20**, 2925-2928.
- Harkrider, D.G. (1964). Surface waves in multilayered elastic media. Part 1. *Bull. Seismol. Soc. Am.* **54**, 627-679.
- Lunedei, E. and Albarelo, D. (2009). On the seismic noise wavefield in a weakly dissipative layered Earth. *Geophys. J. Int.* **177**, 1001-1014. doi:10.1111/j.1365-246X.2008.04062.x.
- Lunedei, E. and Albarelo, D. (2010). Theoretical HVSR curves from full wavefield modeling of ambient vibrations in a weakly dissipative layered Earth. *Geophys. J. Int.* **181**, 1093-1108, doi: 10.1111/j.1365-246X.2010.04560.x.
- Nakamura, Y. (1989). A method for dynamic characteristics estimation of subsurface using microtremors on the ground surface. *Quarterly Report of Railway Technical Research Institute (RTRI)* **30**, 25-33.
- Perton, M., Sánchez-Sesma, F.J., Rodríguez-Castellanos, A., Campillo, M. and Weaver, R.L. (2009). Two perspectives on equipartition in diffuse elastic fields in three dimensions. *J. Acoust. Soc. Am.* **126**, 1125-1130.
- Sánchez-Sesma, F.J. and Campillo, M. (2006). Retrieval of the Green function from cross-correlation: The canonical elastic problem, *Bull. Seism. Soc. Am.* **96**, 1182-1191.
- Sánchez-Sesma, F.J., Pérez-Ruiz, J.A., Campillo, M. and Luzón, F. (2006). The elastodynamic 2D Green function retrieval from cross-correlation: The canonical inclusion problem. *Geophys. Res. Lett.* **33**, L13305, doi:10.1029/2006GL026454.
- Sánchez-Sesma, F.J., Pérez-Ruiz, J.A., Luzón, F., Campillo, M. and Rodríguez-Castellanos, A. (2008). Diffuse fields in dynamic elasticity. *Wave Motion* **45**, 641-654.
- Sánchez-Sesma, F.J., Rodríguez, M., Iturrarán-Viveros, U., Luzón, F., Campillo, M., Margerin, L., García-Jerez, A., Suarez, M., Santoyo, M. A. and Rodríguez-Castellanos, A. (2011a). A theory for microtremor H/V spectral ratio: application for a layered medium. *Geophys. J. Int.* **186**, 221-225.
- Sánchez-Sesma, F.J., Kawase, H. and Matsushima, S. (2011b). Diffuse Fields in Layered Media. Proc. 4th IASPEI / IAEE International Symposium on the Effects of Surface Geology on Seismic Motion. Santa Barbara, California.
- Tamura, S. (1996). Comparison of Body and Rayleigh Wave Displacements Generated by a Vertical Force on a Layered Elastic Medium. Proc. 11th World Conf. on Earthquake Engineering. Paper 1722.
- Tuan, T.T., Scherbaum, F. and Malischewsky, P.G. (2011). On the relationship of peaks and troughs of the ellipticity (H/V) of Rayleigh waves and the transmission response of single layer over half-space models. *Geophys. J. Int.* **184**, 793-800.
- Wang, C.Y. and Herrmann, R.B. (1980). A numerical study of *P*-, *SV*-, and *SH*-wave generation in a plane layered medium. *Bull. Seismol. Soc. Am.* **70**(4), 1015-1036.